Journal Name

ARTICLE

Hole Transporting Materials for Perovskite Solar Cells and A Simple Approach for Determining the Performance Limiting Factors

Received 00th January 20xx,
Accepted 00th January 20xx

DOI: 10.1039/x0xx00000x

www.rsc.org/

Abasi Abudulimu,*[a] Rafael Sandoval-Torrientes,[a] Iwan Zimmermann,[b] José Santos,*[a,c] Mohammad Khaja Nazeeruddin,*[b] Nazario Martín,*[a,c]

The synthesis and characterization of three novel HTMs with different highest occupied molecular orbital (HOMO) energy levels and their performances in $MAPbI_3$-based devices in comparison with Spiro-OMeTAD is reported. Without systematic optimization, the HTMs performed well. The devices delivered fill factors comparable to the one with Spiro-OMeTAD but suffered from short-circuit current. Interestingly, despite the significant differences in HOMO energy levels, all three HTMs generated the same open-circuit voltage (V_{OC}). We explored the performance limiting factors of the HTMs by simple transient photovoltage/photocurrent (TPV/TPC) measurements along with Drift-diffusion simulations. We found no correlation between HOMO energy levels of the HTMs and V_{OC} of the devices. Performances of the devices are limited by high trap density as well as low carrier mobility of the HTMs, and by the shunts present in the devices. Furthermore, the high trap density and low carrier mobility of the HTM are found to induce ion migration effect in the device causing slow decaying components in TPV/TPC . Nevertheless, it is confirmed that J_{SC} and V_{OC}, measured at steady state, are not influenced by the ion migration effect. These HTMs can be improved further by optimizing their conductivity, trap density, morphology, and can be used as alternatives to Spiro-OMeTAD or other expensive, synthetically challenging HTMs. The simple and inexpensive approach presented in this work can also be applied for effectively evaluating charge transporting materials for perovskite solar cells.

Introduction

Hybrid inorganic-organic perovskites have become a hot research topic in the field of photovoltaics due to their broad optical absorption profile, high free charge carrier generation yield, and fast charge carrier mobility.[1] The theoretical maximum power conversion efficiency (PCE) for single-junction perovskite solar cells (PSC) is calculated to be 31%,[2] and over 20% has already been achieved in less than a decade, with the the record performing cell reaching 25.2%.[3] The hole transporting material (HTM) is accredited to be an essential component in achieving such high PCE, as it facilitates carrier extraction and reduces carrier recombination.[4] Spiro-OMeTAD, considered as the benchmark, is the most commonly found HTM in top-performing PSCs. However, several drawbacks still have to be overcome in order to commercialize Spiro-OMeTAD for high-performance PSCs to a large extent. The synthesis of Spiro-OMeTAD is a rather expensive process, and it also needs to be doped with hygroscopic dopants as it does not possess intrinsic high carrier mobility, which in turn decreases the stability of the devices.[5] Thus, developing easy-to-produce, process, scalable, environmentally friendly new HTM is an attractive milestone to achieve.[6-8]

Moreover, there are various reports about the effect of energy levels of both electron and hole transporting materials (ETM and HTM) on the device performance. Those include: (a) certain energy level offsets between perovskite and charge transporting materials (ETM and HTM) are necessary to achieve best device performance;[9-13] (b) while both ETM and HTM help improve fill factor (*FF*), mainly HTM is responsible for the high open-circuit voltage (V_{OC});[14] (c) influence of the HOMO energy level of HTM on the device performance depends on the perovskite applied in the device;[15] (d) V_{OC} is mainly determined by the quasi-Fermi level splitting within the perovskite rather than the energy levels of ETM and HTM.[16-18] Hence, besides finding new suitable HTMs, understanding their role in device physics is also crucial for improving the device performance as well as for advancing the design of PSCs towards commercialization.

Here we report on the synthesis and characterization of three novel HTMs, namely **HTM1**, **HTM2,** and **HTM3** (shown in Figure 1) obtained in two synthetic steps from cheap

[a] *IMDEA Nanociencia, Madrid, 28049, Spain. E-mail: abasi@imdea.org*
[b] *EPFL VALAIS, Sion, 1951, Switzerland.*
[c] *Facultad de Ciencias Químicas, Universidad Complutense de Madrid,28040, Spain.*
†Electronic Supplementary Information (ESI) available: Details of synthesis, compound's spectroscopic and electrochemical characterization, and device's electrical characterization. See DOI: 10.1039/x0xx00000x

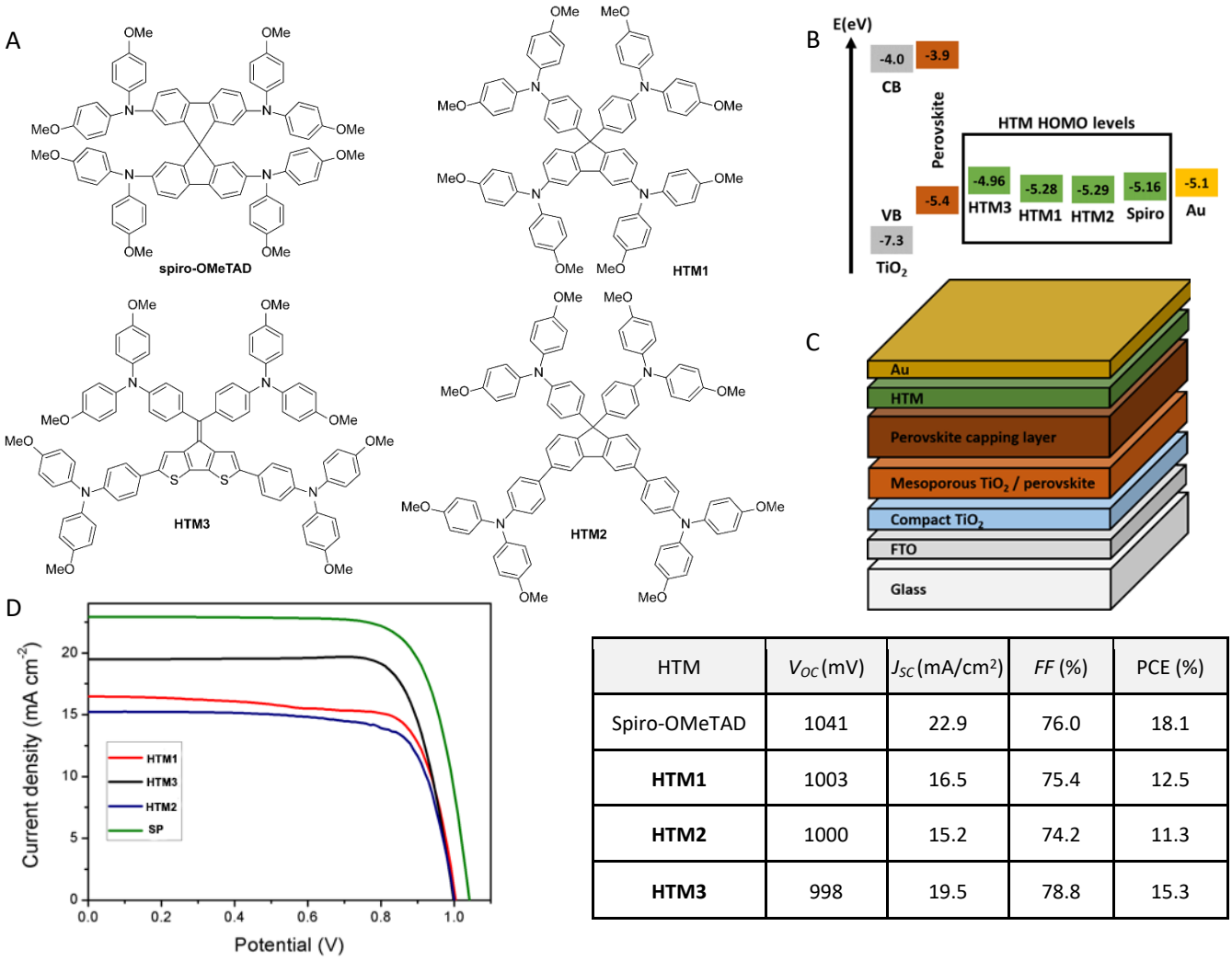

HTM	V_{OC} (mV)	J_{SC} (mA/cm²)	*FF* (%)	PCE (%)
Spiro-OMeTAD	1041	22.9	76.0	18.1
HTM1	1003	16.5	75.4	12.5
HTM2	1000	15.2	74.2	11.3
HTM3	998	19.5	78.8	15.3

Figure 1. (A) Molecular structure of the HTMs. (B) Energy levels of the HTMs estimated by cyclic voltammetry. (C) Device schematics. (D) Representative current-voltage curves of the devices, and (table) their characteristic parameters obtained under one sun illumination.

precursor materials (3,6-dibromofluorenone and 2,6-dibromo-4H-cyclopenta[2,1-b:3,4-b']dithiophen-4-one). We thoroughly studied their performances in the $MAPbI_3$-based PSCs, in comparison with Spiro-OMeTAD. Through current-voltage (J-V) measurements we found that these new HTMs perform quite well, producing *FF* comparable or even exceeding that of the Spiro-OMeTAD. However, they produce less short-circuit current (J_{SC}) than the Spiro-OMeTAD. Moreover, despite the large differences in HOMO levels, we observed that these HTMs resulted in the same V_{OC}. Since any effect of an HTM on the device performance mainly arises either from the desired carrier extraction or undesired carrier recombination, a better understanding of these processes can help to improve designing the HTMs as well as the devices.[1] Therefore, we conducted simple transient Photocurrent (TPC) and transient Photovoltage (TPV) measurements on the devices under various background light intensities to gain a deeper insight on the effect of HTMs on both carrier extraction and recombination dynamics. To confirm the experimental findings, we have also performed drift-diffusion simulations.

Results and Discussion

The chemical core structure of our HTMs (Figure 1A) varies regarding Spiro-OMeTAD in just a single bond (one less), giving rise to hemi-spiro derivatives in the case of **HTM1** and **HTM2**. In addition, we explore the influence of substituting two phenyl rings of the fluorene moiety by two thiophene rings (**HTM3**) on the overall performance, expecting a better interface coupling with the perovskite layer. All these new HTMs are decorated with pendant aryl amine moieties mimicking the benchmark Spiro-OMeTAD (Full synthetic details of the HTMs is disclosed on ESI†).

Based on literature,[10, 13] one may promptly predict from comparison of the HOMO energy levels of the HTMs (shown in Figure 1B) that **HTM3,** with the highest HOMO value, would perform worse as higher interfacial carrier recombination but the same carrier transfer rates are expected when HOMO energy level of the HTM is higher than the valance band of the perovskite. In contrast, **HTM3** actually outperformed the other new HTMs generating the highest J_{SC}, *FF,* and PCE (compare the

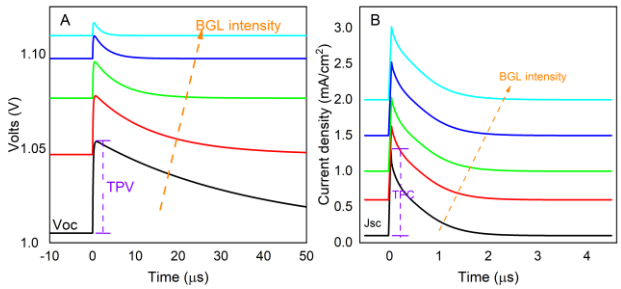

Figure 2. Exemplary TPV (A) and TPC (B) under various BGL intensities.

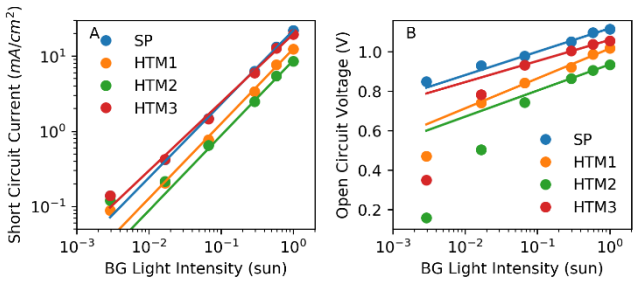

Figure 3. BGL intensity dependence of (A) J_{SC} and (B) V_{OC}, extracted from TPV/TPC data. The solid lines are fits to the last 3-4 measurement points by equation (2) and (4).

electrical parameters and J-V curves in Figure 1). This result suggests that the models for predicting the charge extraction efficiency, and thus, the device performance, should consider not only the relative HOMO energy levels of perovskite and HTM but also their interface coupling.[19] The new HTMs though produced noticeably less J_{SC} and slightly lower V_{OC} than Spiro-OMeTAD. Interestingly, all the new HTMs produced almost identical V_{OC}, despite the large differences in their HOMO energy levels, suggesting no direct connection between HOMO levels of HTMs and V_{OC} of the devices. The simulation results delivered the same conclusion (ESI†). Our findings support the reports which propose quasi-fermi level splitting and carrier recombination inside the perovskite to be responsible for the V_{OC} rather than the energetic levels of the HTMs and ETMs.[16-18]

In order to better understand the performance limiting factors of the HTMs, the charge extraction and recombination dynamics of the devices must be studied in detail, and we performed TPV/TPC measurements for that purpose. It is a simple technique to study devices under operational conditions. Just need to change the load resistance in the measurement system to switch between TPV and TPC, and information such as charge density dependence of carrier recombination and extraction as well as device ideality factor n_{id}, just to mention a few, can easily be obtained by recording the measurement under various background light (BGL) intensity. In addition, light intensity dependence of V_{OC} and J_{SC}, the most common methods to show the recombination mechanism in the device using equation (1) and (2), [20, 21] are already available in the TPV/TPC data, see Figure 2.

$$J_{sc} \propto (BGL)^{a} \quad (1)$$

$$n_{id} = \frac{e}{k_B T}\frac{d(V_{oc})}{d(\log(BGL))} \quad (2)$$

where e is the elementary charge, k_B is the Boltzmann constant, and T is the temperature. The power a, in equation (1), decreases from 1 if bimolecular recombination is significant at short circuit. Though, this method is insensitive to trap-assisted recombination, as both generation G and trap-assisted recombination rates R_{tr} scale linearly with BGL intensity,

$$J_{sc} = ed(G - R_{tr}) = ed(G - k_{tr} n_{tr} n) \quad (3)$$

where d is the active layer thickness, n_{tr} (n) is the trapped (free) charge density, and k_{tr} is the recombination coefficient. Equation (2) results in $1 \le n_{id} \le 2$ depending on the charge carrier recombination mechanism in the devices (n_{id} = 1 if bimolecular recombination dominates and n_{id} = 2 if trap-assisted recombination dominates).

BGL intensity dependence of J_{SC} with a = *1 in* Figure 3A, extracted from TPC data, shows that the devices are free from noticeable bimolecular recombination at short circuit. BGL intensity dependence of V_{OC} in Figure 3B, extracted from TPV data, on the other hand, implies that charge recombination in all these devices at open-circuit is governed by mid-gap or deep traps[21-23] (n_{id} = 2.02, 2.54, 2.22, 1.81 for the devices employing Spiro-OMeTAD, **HTM1**, **HTM2,** and **HTM3**, respectively). Note, the devices with all the new HTMs are affected by shunts resulting in higher slopes in the low light intensity range[23]. Thus, to avoid the influence of shunts on assessing n_{id}, only the last three or four measurement points are fitted in Figure 3B. We have also looked at the differential n_{id} (see ESI†) as well as the n_{id} values derived from TPV transients and come to the same conclusion. The fact that $n_{id} > 2$ for the devices with **HTM1** and **HTM2** may imply presence of ion migration effect[24] or/and of the shunt effects also at higher BGL intensity. Besides the higher slopes at lower BGL intensity range in Figure 3(B), our simulation results (ESI†) also explained that the low shunt resistance is mainly responsible for the lower V_{OC} in the devices fabricated with the new HTMs at one sun compared to the one

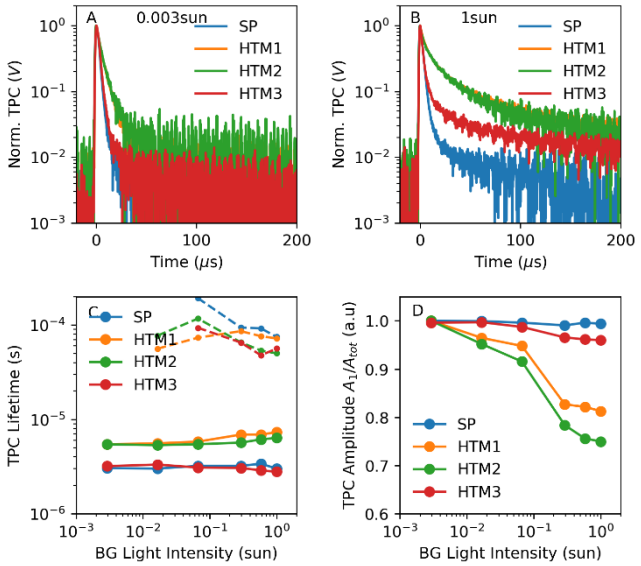

Figure 4. Normalized TPC under 0.003sun (A) and 1sun (B) BGL intensity. (C) BGL intensity dependence of the TPC lifetimes (solid lines for fast component, dashed lines for slow component, acquired by fitting the data to bi-exponential decay function), and (D) their relative amplitudes.

with Spiro-OMeTAD. It might be related to diffusion of Au into the HTMs[21] as the new HTM layers are about 2.3 times thinner than the Spiro-OMeTAD.

TPC results in Figure 4 show that, at low BGL intensity, charge dynamics of the device with **HTM3** at short circuit replicates that of the device with Spiro-OMeTAD. Similarly, charge dynamics of the device with **HTM1** follows that of the device with **HTM2,** revealing the fact that HOMO of the HTM governs the TPC. The differences among them arise as the BGL intensity increases, featuring a slow tail, requiring at least a double-exponential decay function for the fit (see ESI†). The lifetime of the fast component (τ_{TPC}) found to be 3 µs for the devices employing **HTM3** and Spiro-OMeTAD, whereas τ_{TPC} = 6 µs is found for the devices with **HTM1** and **HTM2**. The longer TPC lifetimes in the devices with **HTM1** and **HTM2** are attributed mainly to the lower carrier extraction efficiency of these HTMs arising from their lower carrier mobility compared to Spiro-OMeTAD and **HTM3**. We can neglect the influence of recombination on the TPC of the devices with **HTM1** and **HTM2** as the TPC lifetimes are almost constant over the range of BGL intensity applied in this report (Figure 4C), and at low BGL intensity the charge recombination is at least 10 times slower than the extraction (compare TPC and TPV at low BGL intensity in Figure 4-5). That being said, the carrier mobility is about 5 times slower in **HTM3,** and 10 times in **HTM1**,**2**, compared to Spiro-OMeTAD, according to $\mu = d^2/(2\tau_{TPC}\, V_{bi})$ and $d_{HTM1,2,3} = 0.43 d_{Spiro}$ (where V_{bi} is the built-in potential) when only the HTMs are considered. Consideration of the active layers resulted in mobility values of 5.5, 1.5, 1.6 and 2.8 × 10^{-4} cm^2 V^{-1} s^{-1} for Spiro-OMeTAD, **HTM1**, **HTM2**, and **HTM3**, respectively. Anyhow, TPC of the devices with **HTM3** and Spiro-OMeTAD are slightly affected by carrier recombination at higher BGL intensities (see Figure 4C and Figure 5C).

TPC and its integral ($\int_0^t TPC dt = Q$) should not vary with the BGL intensity if neither the number of charges generated in the perovskite by the weak pulsed light nor the number of charges collected at the electrodes is affected by the BGL intensity. Yet, TPC of all these devices converts from single-exponential decay at low BGL intensity to double-exponential decay at higher BGL intensities. Considering the constant TPC amplitude at all BGL intensity in each device (see ESI†) and the fact that charge generation takes place mainly at the ETL side of the perovskite (see ESI†) within picoseconds with a minor influence of HTM,[1] we can discard the influence of HTMs on the charge generation. Drift-diffusion simulation results illustrated that the slow TPC component could be referred as low carrier mobility or high trap density induced slow charge extraction in the devices (see ESI†). However, when the parameters which guarantee the experimentally observed TPV/TPC characteristics are applied in the simulation, the BGL intensity-dependent TPC features are not well reproduced (see ESI†). It is worth mentioning that the fast TPC components do not react much to the BGL intensity, but the slow components do, resulting in *Q* that fluctuates with BGL intensity as well as with the integration time (see ESI†). We tend to attribute that to the consequence of an ion migration effect, as it is known to act at a time scale longer than the charge extraction time with large contribution from charge traps and

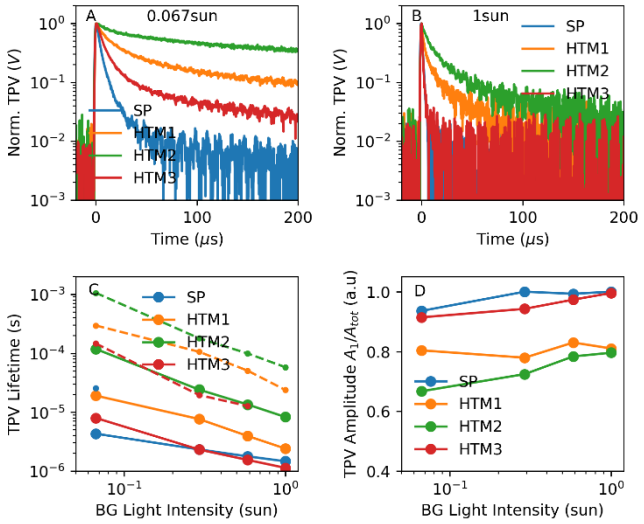

Figure 5. Normalized TPV (A) measured at 0.003sun and (B) 1sun BGL intensities. (C) Lifetimes of fast (solid lines) and slow (dashed lines) TPV components as a function of BGL intensity, attained by fitting the data to double exponential function. (D) The relative amplitude of the fast component.

charge accumulation at the interfaces.[25-27] It explains the more pronounced slow TPC component observed in the devices with **HTM1** and **HTM2**. Charge extraction in these HTMs is slow (Figure 4C), and they possess higher trap density.

TPV data of all the devices exhibit double-exponential decay form at low BGL intensity with around one order of magnitude difference in lifetimes, which are much shorter in the devices with **HTM3** and Spiro-OMeTAD (see Figure 5 and also the fit results in ESI†). The two decay lifetimes have frequently been reported in perovskite solar cells,[22, 25, 26, 28-30] while their origin is still under debate. Some attribute the faster component to the recombination at the perovskite/charge-transporting-material (ETM and HTM) interfaces and the slower component to the recombination within the bulk,[30-32] while others suggest the exact opposite.[25] Figure 5 demonstrates that TPV lifetimes and amplitudes are quite different for devices with different HTMs. This finding may conflict with the claim above, since otherwise, we would have seen at least one of the TPV lifetimes to be the same for all the devices, considering the fact that the devices differ from each other just in the HTM. TPV lifetimes of the slow component also decrease with the increase of BGL intensity, and around one sun the slow component disappears in the devices with Spiro-OMeTAD and **HTM3** while it still takes up to 20% of the total signal in the devices with **HTM1** and **HTM2**. The increase of BGL intensity increases the stationary charge density in the device and consequently reduces the free trap density by filling them up with free charges and can raise the recombination rate. Simulation results demonstrated that both high trap density and slow charge carrier mobility of HTM could extend the TPV lifetime and even can induce a slow decay component (see ESI†). However, the BGL intensity-dependent TPV features are not well reproduced (see ESI†). It is noticed, though, that a moderate trap-density, together with low shunt resistance, is also able to generate the slow TPV component. Nevertheless, it still could not reproduce well the BGL intensity-dependent TPV characteristics observed in the experiment (see

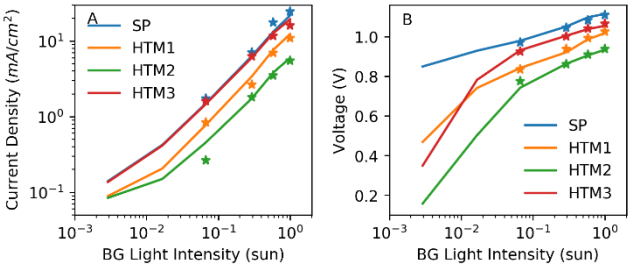

Figure 6. Calculated (A) recombination current and (B) open-circuit voltage as a function of light intensity (symbols). The solid lines are the measured J_{SC} and V_{oc}.

ESI†). The slow TPV component can also be an effect of ion migration as both traps and charge accumulation are known to trigger the ion migration effect in the perovskite solar cells, and at high BGL intensity its effect can be reduced since traps will be filled, and the free charge density in the device will be largely vanished by recombination. Therefore, diminishing of the slow components at lower BGL intensity in the devices with Spiro-OMeTAD and **HTM3**, compared to those with **HTM1** and **HTM2**, denotes the presence of higher trap densities in the **HTM1** and **HTM2** than in the Spiro-OMeTAD and **HTM3**.

Faster TPV and TPC decays are generally referred as to faster charge recombination and faster charge extraction (if recombination in TPC can be neglected), respectively. However, to relate the charge dynamics observed in TPC/TPV to the measured stationary V_{OC} and J_{SC}, one first must confirm whether the TPC/TPV data, at all, represent the charge dynamics that lead to the stationary device performance. For that, we have calculated the recombination current J_{rec} and V_{oc}^{cal} via equation (4) and (5), respectively,[33, 34] using parameters determined solely from TPC/TPV measurements.

$$J_{rec}(V_{oc}\ or\ BGL) = ed\frac{n(V_{oc})}{\tau(V_{oc})} = ed\frac{n(V_{oc})}{\tau_{TPV}(V_{oc})(\lambda+1)} \quad (4)$$

$$n(V_{OC}\ or\ BGL) = \int_0^{V_{oc}} \frac{\int_0^t TPC dt = Q}{\Delta V_{oc}}\, dV = n_0 \exp(\gamma V_{oc}) \quad (5)$$

$$V_{oc}^{cal}(J_{rec}\ or\ BGL) = n_{id}\frac{k_B T}{e}\ln(\frac{J_{sc}}{J_{rec0}}) \quad (6)$$

Where τ is the lifetime of the total charge density n, τ_{TPV} is the TPV lifetime, λ is a constant obtained from τ_{TPV} versus n log-log plot (slope), ΔV_{OC} is the amplitude of the TPV. The ideality factors are calculated as $n_{id} = e/[k_B T\gamma(\lambda+1)]$[33].

We found that the calculated recombination current J_{rec} and open-circuit voltage V_{oc}^{cal} match well with the measured J_{SC} and V_{OC} (Figure 6) when the lifetimes of the fast TPV component and the integral of TPC only up to 3 µs (for the devices with **HTM3** and Spiro-OMeTAD) and 6 µs (for the devices with **HTM1** and **HTM2**) are used in the calculation. The slow TPC component, being not relevant to the stationary $J_{SC,}$ has also been reported recently.[25, 26] Knowing that the charge dynamics represented by the fast TPC/TPV components mainly account for the device performance at steady state, we can now assign the under performances of the devices with the new HTMs, compared to Spiro-OMeTAD, to the higher trap density, slow charge extraction, minor fast carrier recombination (**HTM3**), and to the high shunts present in the devices employing the HTMs. Additionally, an energy barrier (ΔE = 140 meV) between **HTM3** and Au electrode created by their energy levels mismatch cost partial J_{SC}. The J_{SC} increased to 21.0 mA/cm² when the Au electrode was replaced by a Cu one (see ESI†).

Conclusions

In summary, we have synthesized three novel HTMs with different HOMO energy levels and tested their charge extraction performances in $MAPbI_3$ perovskite solar cells in comparison with Spiro-OMeTAD. These HTMs produced *FF* comparable to Spiro-OMeTAD but resulted in noticeably less J_{SC} and slightly lower V_{oc} compared to Spiro-OMeTAD. Interestingly, despite the large differences in the HOMO energy levels, they resulted in the same V_{OC}. By performing TPC/TPV measurements and drift-diffusion simulations, we found that the higher trap density and lower carrier mobility of the HTMs along with the shunts cost the overall performance losses. Higher interfacial carrier recombination and an energy barrier between the HTM and Au electrode partly contributed the performance loss in the device with higher HOMO **HTM3**. Besides, the devices employing HTMs with high trap density and slow carrier mobility showed significant ion migration effect. However, the recombination current J_{rec} and V_{OC} derived from TPV/TPC data confirmed that J_{sc} and V_{oc} measured at steady state are not influenced by the ion migration effect. These HTM have not been systematically optimized yet and can be used as alternatives for some of the expensive and synthetically challenging HTMs by tuning their trap density, conductivity, and morphology, etc. The presented simple approach can efficiently be applied to evaluate HTMs for the photovoltaic devices.

Experimental

Material Synthesis

The synthesis of all HTMs is depicted in Scheme 1. Condensation of 3,6-dibromofluorenone (1)[35] with 4-methoxy-*N*-(4-methoxyphenyl)-*N*-phenylaniline (2)[36] employing Eaton's reagent (7.7% w/w P_2O_5 in $MeSO_3H$) yields fluorene derivative **3** in moderate yield. Subsequent palladium cross-coupling with the appropriate arylamine provides **HTM1** and **HTM2**. The synthesis of **HTM3** is undertaken from 2,6-dibromocyclopenta[2,1-b:3,4-b']dithiophen-4-one (6), which was previously obtained following the procedure described by Wang,[37] by Corey-Fuchs reaction with PPh_3 and CBr_4 to yield compound **7** in moderate yield. The final step is a fourfold Suzuki reaction to couple triarylamine **5**. Detailed synthetic procedures and characterization may be found in the ESI†.

Device preparation

FTO coated glass (NSG10) was sequentially cleaned by sonication in a 2 % Helmanex solution and isopropanol for 15 min, respectively. A 20 nm to 50 nm titania blocking layer was applied on the substrates by spraying a solution of titanium diisopropoxide bis(acetylacetonate) in ethanol at 450 °C. For

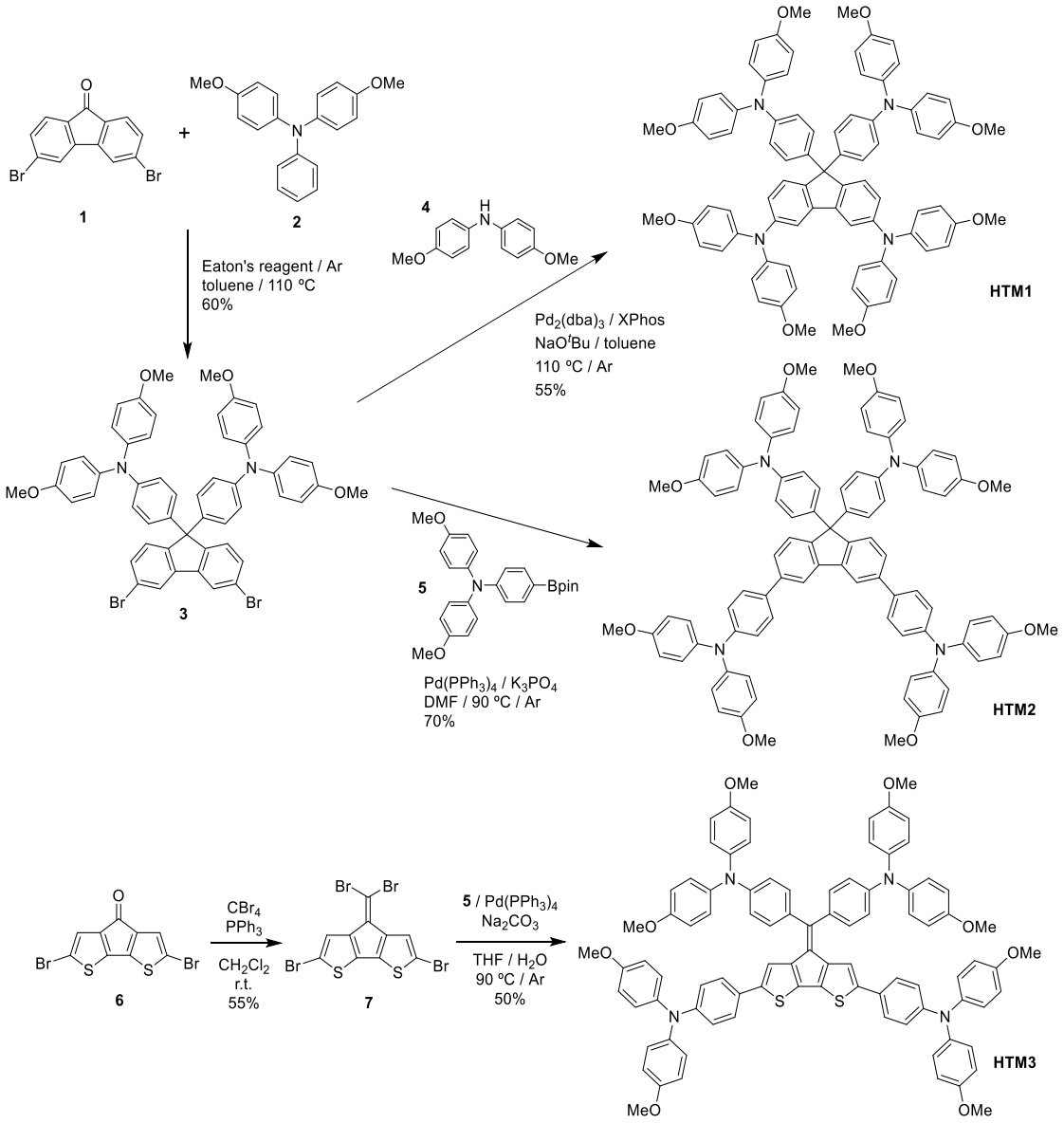

Scheme 1. Synthetic pathways to **HTM1**–**3**.

the 200–300 nm mesoporous TiO_2 layer, 30 NR-D titania paste from Dyesol diluted in ethanol (150 mg/ml) was applied by spin-coating at 4000 rpm for 10 s followed by a sintering step at 500 °C for 30 min. The $MAPbI_3$ perovskite precursor solution was prepared by mixing 461 mg PbI_2 and 159 mg methylammonium iodide in 800 µl of DMSO. The perovskite layers were fabricated by a single step spin-coating procedure reported by Soek *et al.*[38] The perovskite solution was spun at 1000 rpm for 10 s followed by 5000 rpm for 30 s using a ramp of 3000 rpm s^{-1}. 15 s prior to the end of the spin-coating sequence 100 µl of chlorobenzene were poured onto the spinning substrate. Afterwards, the substrates were transferred onto a heating plate and annealed at 100 °C for 45 min. Spiro-OMeTAD (2,2′,7,7′-tetrakis(*N*,*N*-di-p-methoxyphenyl-amine)9,9′-spirobifluorene), **HTM1**, **HTM2** and **HTM3** were used as hole transporting materials and applied from a solution in chlorobenzene. Optimized concentrations were found to be 70 mM for Spiro-OMeTAD and 30 mM for the new HTMs. Tert-butylpyridine (Tbp), Tris(2-(1H-pyrazol-1-yl)-4-tert-butylpyridine)cobalt(III) (FK209) and Tris(bis(trifluoromethylsulfonyl)imide) (Li-TFSI) were added as additives: 330 mol% Tbp, 50 mol% Li-TFSI from a 1.8 M stock solution in acetonitrile and 3 mol% FK209 from a 0.25 M stock solution in acetonitrile. The HTM solution was spin-coated dynamically onto the perovskite layers at 4000 rpm for 20 s. The gold electrodes were deposited by thermal evaporation of 80 nm gold using a shadow mask under high vacuum conditions.

Solar cell I-V characterization

The photovoltaic device performance was analysed using a VeraSol LED solar simulator (Newport) producing one sun AM 1.5 (100 mW cm^{-2}) sunlight. Current-voltage curves were measured in air with a potentiostat (Keithley). The light intensity was calibrated with an NREL certified KG5 filtered Si reference diode. The solar cells were masked with a metal

aperture of 0.16 cm^2 to define the active area. The current-voltage curves were recorded scanning at 20 mV s^{-1}.

TPV/TPC measurements and simulations

The device is connected to a high impedance (1 MΩ) input channel of an Oscilloscope to provide the open-circuit condition. A white LED is used to illuminate the device continuously in the background (BGL) to generate steady-state charge carrier density creating V_{OC}. A weak 532 nm pulsed laser is applied on top of the BGL to create a small number of additional charge carriers (causing an increase in open-circuit voltage, ΔV_{OC}), which decays in time after the light pulse switches off. The rate of the green laser pulse is set to 6 Hz. TPC is the same as TPV, and the only difference is that the device is connected to the oscilloscope's 50 Ω input channel instead of 1 MΩ. Both BGL and pulsed light intensities are controlled by neutral density filters. TPV/TPC signals are recorded with a Picoscope 6424 controlled by a custom-built Python program. The simulation of the TPC/TPV is done by GPVDM software developed by R.C.I. MacKenzie, which models the device parameters by solving the drift-diffusion, carrier continuity, and Poisson's equations.[34] First, the parameters of the model are optimized to reproduce the J-V characteristics of our reference devices with Spiro-OMeTAD. Then, the TPV/TPC are modeled using the same parameters, and only the targeted parameter is allowed to vary when a certain parameter is needed to be swept for a range. The parameters and related results can be found in the ESI†.

Conflicts of interest

There are no conflicts to declare.

Acknowledgments

We thank the European Research Council (ERC-320441-Chirallcarbon), the Spanish Ministry of Economy and Competitiveness MINECO (projects CTQ2014-52045-R, CTQ2014-58801, CTQ2015-71154-P, CTQ2016-81911-REDT, CTQ2017-83531-R, Centro de Excelencia Severo Ochoa SEV-2016-0686 and Unidad de Excelencia María de Maeztu MDM-2015-0538), the CAM (FOTOCARBON project S2013/MIT-2841). We also acknowledge SNSF for financial support of the project "Tailored Design and in-depth understanding of perovskite solar materials using in-house developed 3D/4D nanoscale ion beam analysis, project number: 200020L_1729/1.

References

1. C. S. Ponseca Jr, Y. Tian, V. Sundström and I. G. Scheblykin, *Nanotechnology*, 2016, **27**, 082001.
2. W. E. Sha, X. Ren, L. Chen and W. C. Choy, *Appl. Phys. Lett.*, 2015, **106**, 221104.
3. https://www.nrel.gov/pv/assets/pdfs/best-research-cell-efficiencies.20190802.pdf
4. S. I. Seok, M. Grätzel and N. G. Park, *Small*, 2018, **14**, 1704177.
5. A. Krishna and A. C. Grimsdale, *J. Mater. Chem. A*, 2017, **5**, 16446-16466.
6. I. Garcia-Benito, J. Urieta-Mora, A. Molina-Ontoria, N. Martín, *Chem. Soc. Rev.*, 2018, **47**, 30.
7. L. Calio, S. Kazim, M. Grätzel and S. Ahmad, *Angew. Chem. Int. Ed.,* 2016, **55**, 14522-14545.
8. S. F. Völker, S. Collavini and J. L. Delgado, *ChemSusChem*, 2015, **8**, 3012-3028.
9. I. Zimmermann, J. Urieta-Mora, P. Gratia, J. Aragó, G. Grancini, A. Molina-Ontoria, E. Ortí, N. Martín and M. K. Nazeeruddin, *Adv. Energy Mater.*, 2017, **7**, 1601674.
10. T. Minemoto and M. Murata, *Sol. Energ. Mat. Sol. C.*, 2015, **133**, 8-14.
11. C. Ding, Y. Zhang, F. Liu, Y. Kitabatake, S. Hayase, T. Toyoda, K. Yoshino, T. Minemoto, K. Katayama and Q. Shen, *Nano Energy*, 2018, **53**, 17-26.
12. K.-G. Lim, S. Ahn, Y.-H. Kim, Y. Qi and T.-W. Lee, *Energy Environ. Sci.*, 2016, **9**, 932-939.
13. D. Ompong and J. Singh, *Org. Electron.*, 2018, **63**, 104-108.
14. E. J. Juarez-Perez, M. Wuβler, F. Fabregat-Santiago, K. Lakus-Wollny, E. Mankel, T. Mayer, W. Jaegermann and I. Mora-Sero, *J. Phys. Chem. Lett.*, 2014, **5**, 680-685.
15. S. Ryu, J. H. Noh, N. J. Jeon, Y. C. Kim, W. S. Yang, J. Seo and S. I. Seok, *Energy Environ. Sci.*, 2014, **7**, 2614-2618.
16. M. I. Dar, M. Franckevičius, N. Arora, K. Redeckas, M. Vengris, V. Gulbinas, S. M. Zakeeruddin and M. Grätzel, *Chem. Phys. Lett.*, 2017, **683**, 211-215.
17. J. Jiménez-López, W. Cambarau, L. Cabau and E. Palomares, *Sci. Rep.*, 2017, **7**, 6101.
18. S. Ravishankar, S. Gharibzadeh, C. Roldán-Carmona, G. Grancini, Y. Lee, M. Ralaiarisoa, A. M. Asiri, N. Koch, J. Bisquert and M. K. Nazeeruddin, *Joule*, 2018, **2**, 788-798.
19. J. Shi, A. Isakova, A. Abudulimu, M. van den Berg, O. K. Kwon, A. J. Meixner, S. Y. Park, D. Zhang, J. Gierschner and L. Lüer, *Energy Environ. Sci.*, 2018, **11**, 211-220.
20. C. Ramsdale, J. Barker, A. Arias, J. MacKenzie, R. H. Friend and N. Greenham, *J. Appl. Phys.*, 2002, **92**, 4266-4270.
21. W. Tress, M. Yavari, K. Domanski, P. Yadav, B. Niesen, J. P. C. Baena, A. Hagfeldt and M. Graetzel, *Energy Environ. Sci.*, 2018, **11**, 151-165.
22. D. Bi, L. Yang, G. Boschloo, A. Hagfeldt and E. M. Johansson, *J. Phys. Chem. Lett.*, 2013, **4**, 1532-1536.
23. K. Tvingstedt, L. n. Gil-Escrig, C. Momblona, P. Rieder, D. Kiermasch, M. Sessolo, A. Baumann, H. J. Bolink and V. Dyakonov, *ACS Energy Lett.*, 2017, **2**, 424-430.
24. P. Calado, D. Burkitt, J. Yao, J. Troughton, T. M. Watson, M. J. Carnie, A. M. Telford, B. C. O'Regan, J. Nelson and P. R. Barnes, *Phys. Rev. Appl., **11**, 2018, 044005*.
25. D. Kiermasch, P. Rieder, K. Tvingstedt, A. Baumann and V. Dyakonov, *Sci. Rep.*, 2016, **6**, 39333.
26. B. C. O'Regan, P. R. Barnes, X. Li, C. Law, E. Palomares and J. M. Marin-Beloqui, *J. Am. Chem. Soc.*, 2015, **137**, 5087-5099.
27. A. Abudulimu, L. Lang, L. Guilin, N. Aimaiti, B. Rezek and Q. Chen, *J. Eenergy. Chem*., 2019, https://doi.org/10.1016/j.jechem.2019.12.002
28. S. D. Stranks, V. M. Burlakov, T. Leijtens, J. M. Ball, A. Goriely and H. J. Snaith, *Phys. Rev. Appl.*, 2014, **2**, 034007.

29. R. S. Sanchez, V. Gonzalez-Pedro, J.-W. Lee, N.-G. Park, Y. S. Kang, I. Mora-Sero and J. Bisquert, *J. Phys. Chem. Lett.*, 2014, **5**, 2357-2363.
30. N. r. F. Montcada, J. M. Marín-Beloqui, W. Cambarau, J. s. Jiménez-López, L. Cabau, K. T. Cho, M. K. Nazeeruddin and E. Palomares, *ACS Energy Lett.*, 2016, **2**, 182-187.
31. L. G. Kudriashova, D. Kiermasch, P. Rieder, M. Campbell, K. Tvingstedt, A. Baumann, G. V. Astakhov and V. Dyakonov, *J. Phys. Chem. Lett.*, 2017, **8**, 4698-4703.
32. Y. Li, Y. Li, J. Shi, H. Li, H. Zhang, J. Wu, D. Li, Y. Luo, H. Wu and Q. Meng, *Appl. Phys. Lett.*, 2018, **112**, 053904.
33. A. Maurano, R. Hamilton, C. G. Shuttle, A. M. Ballantyne, J. Nelson, B. O'regan, W. Zhang, I. McCulloch, H. Azimi and M. Morana, *Adv. Mater.*, 2010, **22**, 4987-4992.
34. A. Maurano, C. G. Shuttle, R. Hamilton, A. M. Ballantyne, J. Nelson, W. Zhang, M. Heeney and J. R. Durrant, *J. Phys. Chem. C*, 2011, **115**, 5947-5957.
35. K. Brunner, A. van Dijken, H. Börner, J. J. Bastiaansen, N. M. Kiggen and B. M. Langeveld, *J. Am. Chem. Soc.*, 2004, **126**, 6035-6042.
36. A. C. Hernandez‐Perez, A. Caron and S. K. Collins, *Chem.: Eur. J.*, 2015, **21**, 16673-16678.
37. J. Shi, W. Zhao, L. Xu, Y. Kan, C. Li, J. Song and H. Wang, *J. Phys. Chem. C*, 2014, **118**, 7844-7855.
38. N. J. Jeon, J. H. Noh, Y. C. Kim, W. S. Yang, S. Ryu and S. I. Seok, *Nat. Mater.*, 2014, **13**, 897.